J. Astrophys. Astr. (2006) **27,** 159–166

Initiation of CMEs by Magnetic Flux Emergence

Govind Dubey*, Bart van der Holst† & Stefaan Poedts‡
Centrum voor Plasma Astrofysica, K. U. Leuven, Celestijnenlaan 200 B, 3001 Leuven, Belgium.
**e-mail: govind.dubey@wis.kuleuven.ac.be*
†*e-mail: Bart.vanderHolst@wis.kuleuven.ac.be*
‡*e-mail: Stefaan.Poedts@wis.kuleuven.ac.be*

Abstract. The initiation of solar Coronal Mass Ejections (CMEs) is studied in the framework of numerical magnetohydrodynamics (MHD). The initial CME model includes a magnetic flux rope in spherical, axisymmetric geometry. The initial configuration consists of a magnetic flux rope embedded in a gravitationally stratified solar atmosphere with a background dipole magnetic field. The flux rope is in equilibrium due to an image current below the photosphere. An emerging flux triggering mechanism is used to make this equilibrium system unstable. When the magnetic flux emerges within the filament below the flux rope, this results in a catastrophic behavior similar to previous models. As a result, the flux rope rises and a current sheet forms below it. It is shown that the magnetic reconnection in the current sheet below the flux rope in combination with the outward curvature forces results in a fast ejection of the flux rope as observed for solar CMEs. We have done a parametric study of the emerging flux rate.

Key words. Sun: corona, coronal mass ejections—magnetic fields—magnetohydrodynamics—flux emergence.

1. Introduction

Coronal Mass Ejections (CMEs) play a *crucial role* in space weather and a careful study of the origin, structure, and propagation characteristics of this violent phenomenon is essential for a deeper insight into space weather physics. The fast CMEs are important because of the geomagnetic storms created by the impact of the CMEs on the earth's magnetosphere and the solar energetic particles (SEPs) accelerated by the CME leading shock front. Clearly, the theoretical modelling of the evolution of CMEs can be divided into sub-problems. An important unresolved sub-problem is the initiation of CMEs, i.e., the question why CMEs occur at all and how are they triggered?

Klimchuk (2001) reviewed the theoretical models for CME initiation. Based on basic physical properties such as energetics, structure and dynamics, this author distinguished two types of models, viz., *directly driven* models and *storage and release* models. However, *all these models have difficulty explaining one or more aspects of observations.* Hence, a lot of work remains to be done to improve the present models: 3D extensions need to be created including fine structure, real (i.s.o. numerical) dissipation, a realistic shearing of foot points, etc. CME shock evolution studies very often

apply *simplified* generation models for CMEs. Groth *et al.* (2000) used a 'density-driven' model which simply means that a high-density (and high-pressure) plasma blob is superposed on the solar wind. Other simplified models generate a pressure pulse with or without an additional velocity change (i.e., a kind of 'nozzle' boundary condition), see e.g., Wang *et al.* (1995) and Odstrcil & Pizzo (1999). Keppens & Goedbloed (1999), on the other hand, impose an extra mass flow to generate CMEs.

More realistic CME evolution simulations make use of theoretical analytic CME initiation models such as the models of the self-similar Gibson & Low (1998) family (Gombosi *et al.* (2000)) or the Titov & Démoulin model (Roussev *et al.* (2003)). Odstrcil & Pizzo (2002) and Odstrcil *et al.* (2003) use yet another analytical flux rope model. What one should really do, however, is to simulate the evolution of the reconstructed coronal structures (e.g., Aulanier *et al.* (2000)) driven unstable by foot point shearing and/or flux emergence or cancellation. Several groups are working on such simulations and results will appear in the near future.

The CME initiation model presented in this paper extends earlier results obtained by Lin *et al.* (1998) and Chen & Shibata (2000) by including geometry effects (curvature) and gravitational stratification, and performing a parametric study.

2. Model and numerical method

2.1 *Initial model*

Our pre-CME model is motivated by the work of Chen & Shibata (2000) and Lin *et al.* (1998). Chen & Shibata used three separate line current elements to get the detached magnetic flux rope in a 2D cartesian plane. We have also considered three separate current elements but in a 2.5D spherical plane: a ring current centered at distance h above the photosphere on the equator with a finite radius r_0, its image current is located below the photosphere, and a background dipole field, similar to that in Forbes (1990). In the present work, we do not consider the formation of flux ropes but in previous studies, several mechanism have been suggested for this.

We use spherical coordinates (r, θ, φ) and express the magnetic field $\mathbf{B}$ in terms of a vector potential A_φ, i.e., $\mathbf{B} = \nabla \times (A_\varphi \mathbf{e}_\varphi) + B_\varphi \mathbf{e}_\varphi$. The initial magnetic configuration is given by $A_\varphi = A_{\varphi r} + A_{\varphi i} + A_{\varphi b}$, where the magnetic vector potential of the ring current ($A_{\varphi r}$), its image current ($A_{\varphi i}$) and the background dipole field ($A_{\varphi b}$) have the following forms:

$$A_{\varphi b}(r,\theta) = m\frac{\sin\theta}{r^2}, \tag{1}$$

$$A_{\varphi r}(r,\theta) = \begin{cases} \frac{4Ih}{\sqrt{h^2+r^2+2hr\sin\theta}}\ \frac{[(2-k_1^2)K(k_1)-2E(k_1)]}{k_1^2} & r_1 > r_0 \\ B_0\ \frac{j_0(\lambda r_1)}{\lambda r\sin\theta} & r_1 \le r_0, \end{cases} \tag{2}$$

$$A_{\varphi i}(r,\theta) = -\frac{4IhR_0}{\sqrt{r^2h^2+R_0^4+2hrR_0^2\sin\theta}}\frac{[(2-k_2^2)K(k_2)-2E(k_2)]}{k_2^2}, \tag{3}$$

where m is the dipole strength in the formula of background field, j_0 is a Bessel function of zeroth order, $r_1 = \sqrt{r^2+h^2-2rh\sin\theta}$ is the radial distance from the

flux rope center, K and E are the complete elliptic integrals of the first and second kind, respectively, and

$$k_1^2 = \frac{4hr\sin\theta}{h^2 + r^2 + 2hr\sin\theta}, \qquad k_2^2 = \frac{4hrR_0^2\sin\theta}{h^2r^2 + R_0^4 + 2hrR_0^2\sin\theta}.$$

The constant λ is chosen such that $j_0(\lambda r_0 = 0)$. Moreover, we consider a flux rope with radius $r_0 = 0.1\ R_\odot$ at a distance $h = 1.3\ R_\odot$ from the solar center (i.e., $0.3\ R_\odot$ above the photosphere). The strength of the magnetic field in the center of the flux rope is chosen as $B_0 = 5.6$ G.

We assume axial symmetry in our model and that there are no magnetic field sources at infinity. The current within the flux rope, that is located at the equatorial plane, is the only current source within the region $r > R_\odot$ prior to the eruption.

We have taken into account the effect of gravity in our model. As a result, the ambient density is stratified, i.e., $\rho_g = \exp(((v_{\rm esc}^2/r) - 1)/2)$, where $v_{\rm esc}$ is the escape velocity of the Sun. The flux rope is initialized with a high density that is distributed as:

$$\frac{\rho}{\rho_0} = \begin{cases} \rho_g + \dfrac{2\ \cos\pi r_1^2}{\beta(2r_0)^2} & r_1 \le r_0 \\ \rho_g & r_1 > r_0. \end{cases} \tag{4}$$

An initial uniform temperature is assumed $T = T_0$ and the initial velocity $\mathbf{v}$ is set to zero. The initial distribution of the electric current density and magnetic field inside the flux rope is arbitrary to some extent. The initial state is iteratively relaxed to a numerically satisfied equilibrium state before the flux triggering mechanism is applied.

2.2 *Numerical methods*

The 2.5D (axially symmetric) time dependent ideal MHD equations are applied. This set of PDEs is solved numerically by means of the VAC Code (Versatile Advection Code, Toth (1996)) by a two-step Runge-Kutta scheme in time and for the spatial discretization we use a second order finite volume scheme, viz., the TVD Lax-Friedrichs method. The solenoidal condition, $\nabla\cdot\mathbf{B} = \mathbf{0}$, is maintained to machine precision using Balsara's (2003) approach.

We have taken the following characteristic values for normalizing the density and temperature: $\rho_0 = 1.6726\times10^{-16}$ g/cm^3, and $T_0 = 1.5\times10^6$ K, respectively. The solar radius $R_\odot = 6.9626\times10^{10}$ cm is used to normalize the length scales. The numerical units for the other quantities follow from these, viz., velocity $v_0 = T_0 2k_b/m_p = 15.74\times10^6$ cm/s, time $t_0 = R_\odot/v_0 = 4420$ s, $B_0 = v_0\sqrt{4\pi\rho_0} = 0.7216$ Gauss, and magnetic flux $\psi_0 = B_0R_\odot^2 = 34.98\times10^{20}$ Mx. We have considered ideal MHD but reconnections of magnetic field lines can occur due to the numerical diffusion. In the near future, we will take into account finite magnetic resistivity in our model.

The computational domain is part of the (r,θ)-plane limited by $1 \le r \le 30$ and $0 \le \theta \le \pi$. This domain is discretized by 600×201 grid points, which are non-uniformly distributed in both the r-and θ-directions. The numerical grid is accumulation near $r = 1$ and $\theta = \pi/2$ with a stretch factor of 50 and 10 in the r- and θ-directions, respectively. The bottom boundary of the simulation area is a line tying boundary,

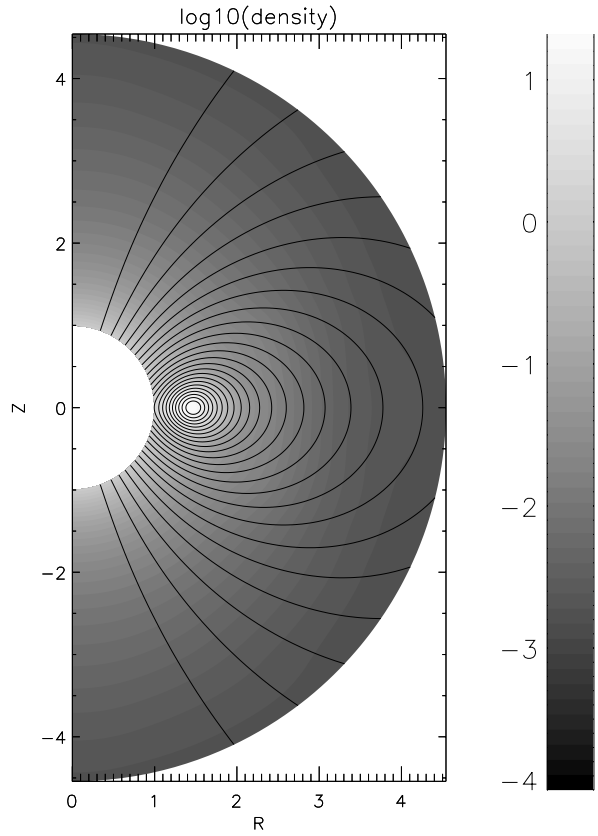

Figure 1. The plasma density $\log_{10} \rho$ (grey scale) and magnetic field lines for the initial relaxed configuration (i.e., at $t = t_0 = 32.0$ or 39.3 hours).

where all quantities except the temperature T are fixed outside the flux emergence region, while T is determined by equivalent extrapolation. The boundary conditions at the poles for the φ- and θ-components of vector quantities are asymmetric, while for the r-components and the plasma density symmetric BCs are applied.

The simulations are done in two phases. In an initial phase the initial state is relaxed for a long period, viz., until $t = 32$ corresponding to 39.3 hours, to assure that a numerical equilibrium is reached with a stable flux rope, see Fig. 1. After this initial phase the kinetic energy of the system and the changes in density and magnetic fields are negligible. Note, that in equations (2) and (3), the current I has been determined by trial and error to make sure that the flux rope center approximately keeps stable for a long enough time, viz., 32 time units. In these simulations the (dimensionless) value of I we obtained this way is 6.33.

In analogy with Forbes *et al.* (1984) and Chen & Shibata (2000), the magnetic flux emergence is then implemented by changing the boundary magnetic field in time. This is done by changing the value of vector potential A_φ starting at $t = t_0 = 32$. The magnetic flux emergence region is limited to $\pi/2 - 0.6 \leq \theta \leq \pi/2 + 0.6$ and grows

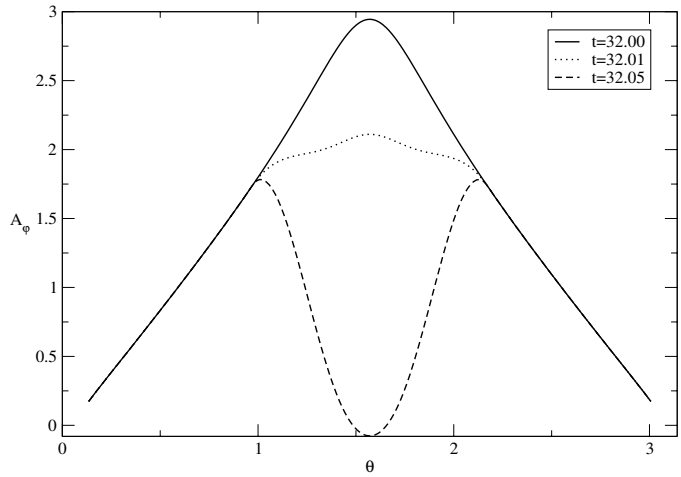

Figure 2. $A_\varphi\big|_{r=1}$ versus θ at $t = t_0 = 32.0$ (after the relaxation), $t = 32.01$ (during the flux emergence), and $t = 32.05$ (after the flux emergence).

linearly in time, in the time interval $\Delta t = t_e - t_0$:

$$A_\varphi(t;\theta)|_{r=1} = A_\varphi(0;\theta)|_{r=1} + c_e \frac{(t-t_0)}{\Delta t} \frac{\cos^2\left(\left(\frac{\pi}{2}-\theta\right)\frac{\pi}{1.2}\right)}{\sin\theta}, \quad t_0 \le t \le t_e, \qquad (5)$$

where c_e is a free parameter. This BC is illustrated in Fig. 2. After $t = t_e$ all quantities at the bottom boundary are again fixed (except for the value of T) as before.

3. Numerical results

After the initial relaxation of the equilibrium (as described above) the triggering phase starts. In this phase we emerge the magnetic flux at the lower boundary ($r = 1$) in a limited time interval ($\Delta t = t_e - t_0$) and a limited θ-interval around the equator. We considered a range of different time intervals, i.e., different values of the parameter t_e in equation (5). The parameter c_e in equation (5) is set to -3 in all simulations so that the total amount of emerged flux is the same in all simulations, viz., $2\pi\ c_e\ \psi_0 \approx -6.6\times10^{20}$ Mx in northern hemisphere and the exact opposite in the southern hemisphere. Hence, we effectively change the *flux emergence rate*, i.e., $2\pi\ c_e\ \psi_0/\Delta t$, in this parametric study as the same amount of flux is emerged in a time interval ranging from 0.05 to 3, i.e., from 221 s to 3 h 41 min. The flux emergence rate thus varies from -3×10^{18} Mx/s to -5×10^{16} Mx/s. Note that the emerging magnetic flux has the opposite polarity from the ambient coronal magnetic field.

As the new magnetic flux emerges near the neutral line magnetic reconnections take place below the flux rope leading to partial magnetic cancellation and the loss of equilibrium. Consequently, the flux rope starts moving upwards and the region below the flux rope is evacuated and suffers a pressure drop. Therefore, magnetized plasma at both sides (left and right to the null point) is seen to move inward. A clearly formed current sheet below the flux rope can be seen in Fig. 3. The current in the sheet has the same direction as that in the flux rope and, therefore, flux rope feels a downward Lorentz force because of this sheet current. With a finite resistivity, the current sheet

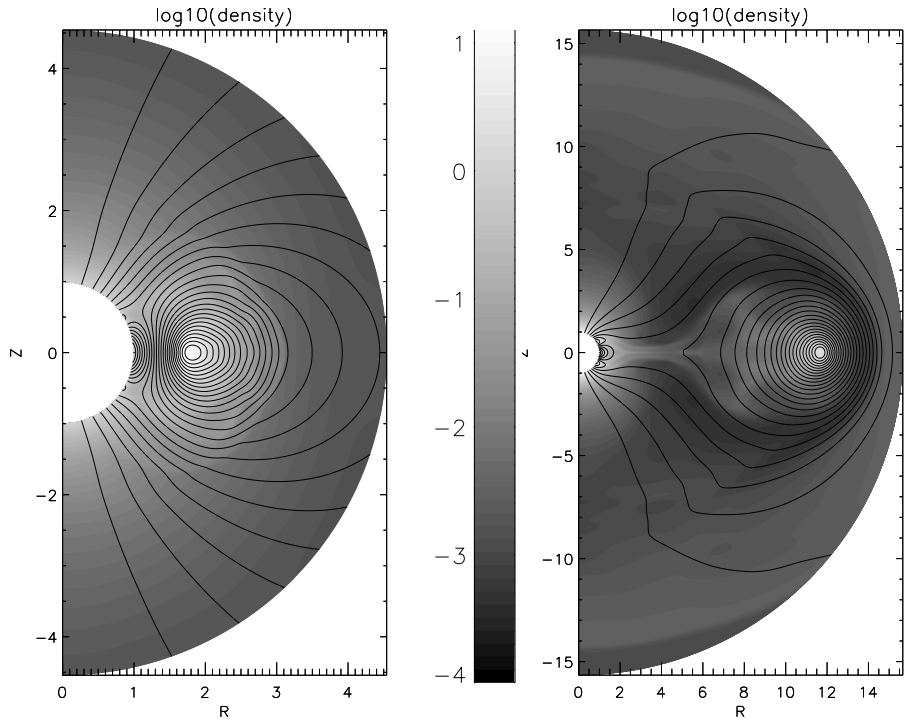

Figure 3. The plasma density $\log_{10}\rho$ (grey scale) and magnetic field lines at $t = 32.3$ (left) and at $t = 36.0$ (right, with a different scale on the abscissa) for the case with $t_e = 32.05$.

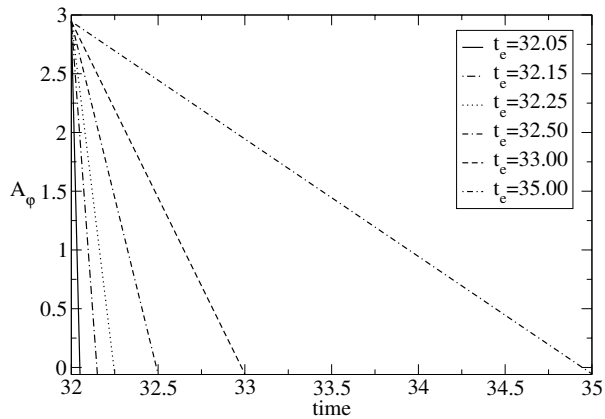

Figure 4. Considered time dependencies of $A_\varphi\big|_{r=1,\theta=\frac{\pi}{2}}$ for the same c_e value ($= -3$).

would be dissipated and the escaping flux rope would be accelerated in that case. Here however, we only rely on numerical diffusion.

We have performed a parametric study of the emerging flux rate by changing the value of t_e while keeping c_e constant. This is illustrated in Fig. 4. The corresponding

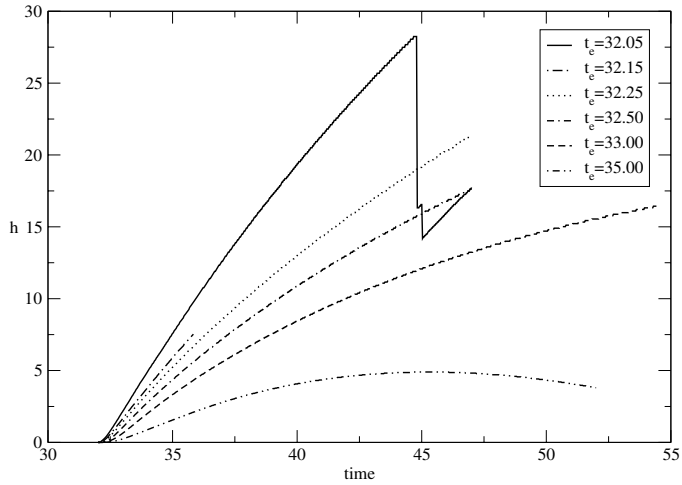

Figure 5. Height of the flux rope center vs. time for the different flux emergence rates.

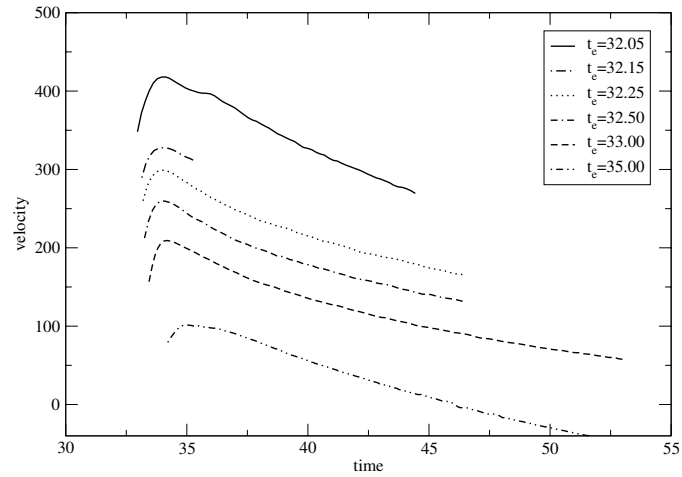

Figure 6. Velocity of the flux rope center vs. time for different flux emergence rates.

height-time curves of flux rope center are shown in Fig. 5. From these curves, the velocities can be easily derived. The related velocities are shown in Fig. 6. Clearly, an increasing flux rate leads to a higher upward speed of the flux rope while the total amount of emerged flux is the same in all cases. The obtained velocities are in the range which is typical for CMEs. For an emerging flux rate that is smaller than some threshold value, the flux rope cannot escape from the corona and it falls down again as a result of the deceleration due to gravity (see e.g., the lowest curve in Fig. 5).

4. Discussion and conclusion

The CME initiation model of Chen & Shibata (2000) has been extended by including the effects of gravity, geometry (curvature), and an ambient medium. Moreover, we studied the effect of the flux emergence rate on the velocity of the resulting flux rope CMEs. The obtained velocities lie in the typical range of 300–400 km/s for reasonable values of the flux emergence rate. For smaller values of the flux emergence rate, the launched flux rope falls back to the Sun as a result of the gravitational deceleration. The present model cannot explain fast CMEs. Yet, these fast CMEs are the important ones for space weather, since these CMEs drive shocks which accelerate particles and impinge on the Earth's magnetosphere. In future analyses we will extend the parametric study to investigate whether we can simulate the deceleration of the fast CMEs and the acceleration of slow CMEs as observed by Gopalswamy (2004). Furthermore, we will include the effect of the drag of the background solar wind.

Acknowledgements

These results were obtained in the framework of the projects GOA 2004/01 and OT 02/57 (K. U. Leuven) and G.0451.05 (FWO-Vlaanderen).

References

Aulanier, G., DeLuca, E. E., Antiochos, S. K. *et al.* 2000, *ApJ*, **540**, 1126–1142.
Balsara, D. S. 2001, *J. Comp. Phys.*, **174**, 614.
Balsara, D. S. 2003, *Astrophys. J. Supplement Series*, **151**, 149.
Chen, P. F., Shibata, K. 2000, *Astrophys. J.*, **545**, 524.
Forbes, T. G. 1990, *J. Geophys. Res.*, **95**, 119,19.
Forbes, T. G., Isenberg, P. A., Priest, E. R. 1994, *Solar Phys.*, **150**, 245.
Forbes, T. G., Priest, E. R. 1995, *Astrophys. J.*, **446**, 377.
Gibson, S. E., Low, B. C. 1998, *Astrophys. J.*, **493**, 460.
Gombosi, T. I., DeZeeuw, D. L., Groth, C. P. T., Powell, K. G., Stout, Q. F. 2000, *J. Atm. S-T Phys.* **62**, 1515–1525.
Gopalswami, N. 2004, In: "The Sun and the Heliosphere as an Integrated system", ASSL series, (eds) Poletto, G., Suess, S., Kluwer/Boston, Chapter 8, p. 201.
Groth, C. P. T., DeZeeuw, D. L., Gombosi, T. I., Powell, K. G. 2000, *J. Geophys. Res.*, **105**, 250,53–250,78.
Keppens, R., Goedbloed, J. P. 1999, *A & A*, **343**, 251–260.
Klimchuk, J. A. 2001, Proc. of the Chapman Conference on Space Weather, AGU, Geophysical Monograph Series 125, (eds) Song, P., Singer, H., Siscoe, G., 143–157.
Lin, J., Forbes, T. G., Isenberg, P. A., Demoulin, P. 1998, *Astrophys. J.*, **504**, 1006.
Liu, Y., Jiang, Y., Haishen, J., Zhang, H., Wang, H. 2003, *Astrophys. J.*, **593**, 137.
Mikic, Z., Linker, J. A. 1994, *Astrophys. J.*, **430**, 898.
Odstrcil, D., Pizzo, V. J. 1999, *J. Geophys. Res.*, **104**, 483–503.
Odstrcil, D., Pizzo, V. J. 2002, *ESA*, **SP-477**, 293–296.
Odstrcil, D., Vandas, M., Pizzo, V. J., MacNeice, P. 2003, *American Institute of Physics*, **679**, 699–702.
Roussev, I. I., Forbes, T. G., Gombosi, T. I., Sokolov, I. V., DeZeeuw, D. L., Birn, J. 2003, *ApJ*, **588**, L45–L48.
Tóth, G. 1996, *Astrophys. Lett. Comm.*, **34**, 245.
Wang, A. H., Wu, S. T., Suess, S. T., Poletto, G. 1995, *SPh*, **161**, 365–381.